A Unified Modeling Approach to Tapped Inductor Converters Accounting for the Leakage Inductance Effects

Jia Yao, *Member, IEEE*, Kewei Li, Kaisheng Zheng, and Alexander Abramovitz

***Abstract*—This article suggests a unified modeling approach to the analysis of tapped-inductor converters. The leakage inductance, inherent to coupled magnetic structures, and the associated snubber circuit effects were considered and incorporated into the suggested model. The proposed nonideal tapped inductor switcher model is formulated as an equivalent subgraph that can help to model most, if not all, converter topologies that comprise a two-winding tapped inductor. Both the continuous current mode and the discontinuous current mode were modeled. To validate the proposed approach, analysis of a Flyback converter with an *RC* snubber is presented. Theoretical prediction of the steady-state and small-signal behavior of the converters were confirmed by simulation and experimental results.**

***Index Terms*—DC/DC converter, leakage inductance, small-signal modeling, tapped inductor (TI), unified modeling cell.**

I. Introduction

TAPPED inductor (TI) converters can attain a wider voltage conversion ratio than their basic counterparts [1], [2]. This desirable feature makes TI converters an attractive solution to numerous industrial and consumer applications, particularly in the field of alternative energy generation systems, where high voltage step-up is needed [2], [3].

A practical TI, as any other magnetic device, creates a certain amount of magnetic field outside the magnetic core [4]. The leakage magnetic field stores energy and manifests itself as a leakage inductance in series with the primary and the secondary windings, see Fig. 1. Magnetic designers seek to minimize the leakage inductance by application of special winding techniques [5]–[7]. These can help limit but, not to entirely eliminate the leakage problem. Hence, practical coupled magnetic devices always comprise some amount of leakage. Although the leakage inductance is small compared to the magnetizing inductance, it impairs the switching processes within a switched circuit. For this reason, applying TI poses several challenges.

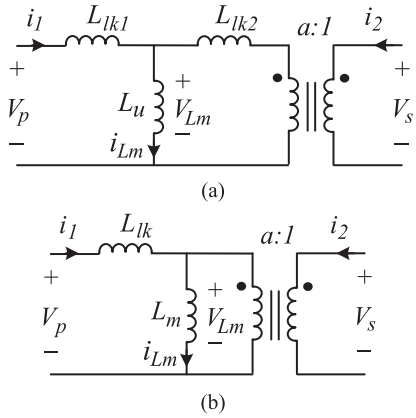

Fig. 1. Coupled magnetic device models (excluding the winding and core losses). (a) T-model. (b) Cantilever model [4].

The leakage inductances can oscillate with the parasitic switch capacitance creating high voltage spikes across the semiconductors. To minimize such "ringing" the energy stored in the leakage inductance has to be safely discharged. This calls for the application of various solutions such as resistor-capacitor-diode (RCD) clamp [4], lossless regenerative snubbers [8], [9], soft switching techniques [10], or active clamp circuits [15].

In course of the converter's operation, the leakage inductance charging and discharging processes introduce current commutation intervals. As a result, additional topological states appear, which somewhat affect both the steady-state and small-signal behavior of the power stage. Therefore, the operation and, consequently, analysis and design of TI converters become more complex.

As an example, the simulated frequency response plot of a Flyback converter, illustrated in Fig. 2, suggests that the leakage inductance affects the damping factor of the converters' small-signal frequency response functions. As a result, a difference in between the resonant peak and phase transitions can be observed. Earlier counterparts considered the impact of the leakage on the steady-state solution [12], [13], and on small-signal behavior [14], [15]. However, the improvement is limited due to the lack

Manuscript received 25 April 2021; revised 13 October 2021, 26 December 2021, and 19 March 2022; accepted 19 April 2022. Date of publication 26 April 2022; date of current version 26 July 2022. This work was supported by the National Natural Science Foundation of China under Grants 51707096 and 51977111. Recommended for publication by Associate Editor D. Vinnikov. *(Corresponding author: Jia Yao.)*

Jia Yao, Kewei Li, and Kaisheng Zheng are with the Department of Electrical Engineering, School of Automation, Nanjing University of Science and Technology, Nanjing 210094, China (e-mail: yaojia@njust.edu.cn; likewei9703164@163.com; zks471945188@gmail.com).

Alexander Abramovitz is with the Department of Electrical Engineering, Holon Institute of Technology, Holon 58102, Israel (e-mail: alabr@hotmail.com).

Color versions of one or more figures in this article are available at https://doi.org/10.1109/TPEL.2022.3170448.

Digital Object Identifier 10.1109/TPEL.2022.3170448

TABLE I
COMPARISON OF MODELING METHODS OF PWM DC–DC CONVERTERS WITH TRANSFORMER/TAPPED INDUCTOR CONVERTERS

Ref. No.	Model type	Considering leakage	Small-signal model	Unified model	CCM/DCM	Clamp circuit type
[11]	Analytical	No	Yes	No	CCM	No
[19]	Anal. & Sim.	No	Yes	Yes	CCM	No
[20]	Analytical	Yes	Yes	Partially	CCM	Passive clamp + quasi-resonant
[21]	Analytical	Yes	Yes	No	CCM	Passive clamp + quasi-resonant
[23]	Analytical	Yes	Yes	Yes	CCM	Active snubber
[24], [25]	Simulation	Yes	No	Yes	Both	Lossy clamp
[26]	Simulation	Yes	Yes	Partially	CCM	Lossy clamp
Proposed approach	Analytical	Yes	Yes	Yes	Both	Lossy clamp

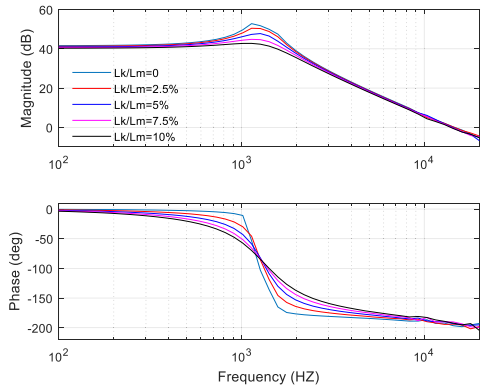

Fig. 2. Simulated control-to-output frequency response of a Flyback converter with RCD clamp for different values of the leakage inductance. (Magnetizing inductance $L_m = 600$ μH; leakage inductance: L_k:(0%–10%); input voltage, $V_{\text{in}} = 120$ V; turns ratio: 4:1, duty cycle $D = 0.5$; $f_s = 65$ kHz, $V_{\text{out}} \approx 30$ V. Simulated by PSIM v.9.14).

of consideration of the snubber circuit's effects [16], [17]. Due to the different operating principles of the various snubbers, the modeling can vary significantly [18]–[25]. The reduced-order generalized averaging method was proposed in analyzing the resonant soft-switching half-bridge converter in [18]. A unified pulsewidth modulation (PWM) switch model for dc-dc converter with the coupled inductor is proposed in [19] however, without considering the leakage inductance. While a generalized PSPICE model for a family of Flyback/boost derived dc–dc converters with clamp circuit was proposed in [20]. A reduced order averaged model for Boost/SEPIC derived dc–dc converter with coupled inductor and passive snubber was proposed in [21]. Also, small-signal model of the Flyback converter with RCD snubber was derived in [26], however, cannot be applied to a different topology.

The modeling of converters with active snubber was also studied. In [22], an averaged model based on time-scale separation of converter state variable was proposed, while a unified small-signal model of a generalized switch network for active clamp was presented in [23]. As shown in this study, the frequency response of a Flyback converter with an *RC* clamp is different from an active clamp circuit [23]. The technique of modeling the lossy snubber circuit, such as *RC* clamp, was also suggested [24]–[26]. A unified five terminal behavioral PSPICE model which considered the leakage inductance was proposed in [24] and [25] for simulation purposes. However, the model cannot provide analytical solutions, such as transfer functions. Analysis of a nonideal Flyback converter with an RCD clamp was produced by [26], which attained the small-signal transfer function of the converter. Yet, the analysis lacks the generalization to other TI topologies. The unified model [27], [28] were all concerned with a simple inductor cell, thus, do not consider the leakage effect.

Comparison of the mentioned modeling approaches, shown in Table I, implies that no unified analytical modeling method for PWM converters comprising transformer/tapped inductor which considers the impact of leakage inductance on small-signal behavior of converters has been reported yet. Moreover, the DCM operational mode was mostly overlooked in the earlier literature.

The recently proposed tapped inductor switcher (TIS) model was suggested to facilitate unified analysis of PWM converters with TI or simple inductor [29]. However, Abramovitz *et al.* [29] treated only ideal (leakage-less) TI converters in continuous current mode (CCM). In this article, TIS modeling approach is further extended to account for the effect of the leakage inductance on the TI converters' steady-state voltage conversion ratio as well as on its small-signal transfer functions in both CCM and discontinuous current mode (DCM) operational conditions. The proposed models are general and can be applied to most two-winding TI converter topologies.

To verify the proposed model, an analysis example of Flyback converter is presented. Simulation and experimental results are compared to the theoretical predictions derived from the proposed model and stand in good agreement.

II. DERIVATION OF THE TIS_C MODEL

A. TIS_C Equivalent Circuit Topology

The tapped inductor switcher (TIS) block was identified as an invariant building block of TI PWM converters. A detailed

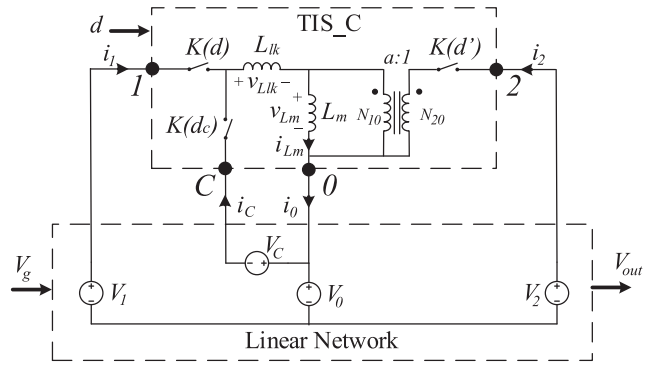

Fig. 3. Improved Tapped Inductor Switcher (TIS_C) incorporates the leakage of the tapped inductor, L_{lk}, and the clamp/discharge terminal *C*.

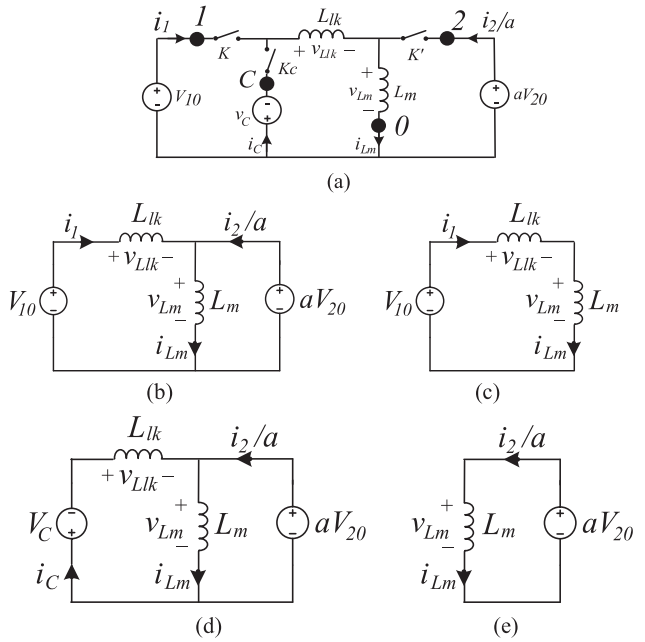

Fig. 4. Tapped inductor switcher with the load reflected to primary (CCM model). (a) Schematic diagram. (b) TIS_C equivalent circuits during the ON commutation interval. (c) ON-state. (d) OFF commutation interval. (e) OFF-state.

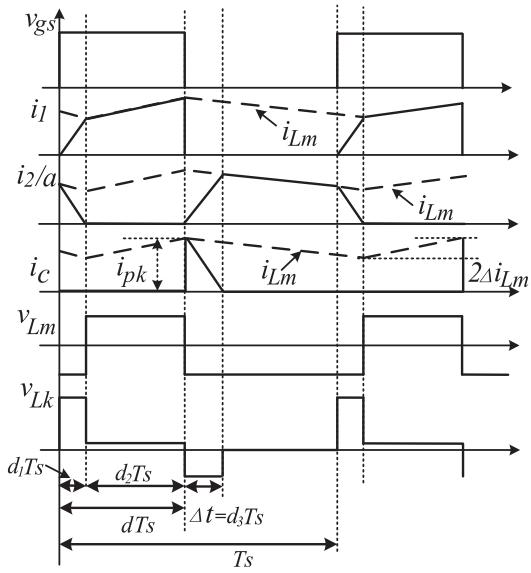

Fig. 5. Key waveforms of the Tapped inductor switcher in current continuous mode (CCM). (*Vc* represents the clamp voltage).

procedure for finding the equivalent parameters of the TIS model was given in [29] and in the sake of brevity will not be restated here. The original TIS model assumed a negligible leakage; however, such an assumption may not always be justified. Therefore, a more accurate model is desirable. The proposed tapped inductor switcher (TIS_C) incorporates the leakage of the tapped inductor, L_{lk}, and the clamp/discharge terminal C as illustrated in Fig. 3. Identification of the TIS_C within several converter topologies is shown in the Appendix.

1) State Analysis and Basic Assumptions: The equivalent circuit of TIS_C with the secondary side referred to the primary is shown in Fig. 4(a). Here, the transformer's winding ratio is defined as $a = N_{10}/N_{20}$ [29]. Key TIS_C waveforms, shown in Fig. 5, illustrate the effect of the leakage on the operation of a TI converter.

First, the leakage is responsible for the appearance of current commutation intervals. Second, the leakage discharge current, i_c, flows through the C terminal upon turn-OFF of the K switch and turn-ON of the K_C switch. Third, the volt-sec needed to develop the leakage current are taken from of the magnetizing inductance L_m. Accordingly, in CCM, in the presence of leakage, the switching cycle is comprised of four topological states. The equivalent circuits of the equivalent subtopologies are illustrated in Fig. 4.

In the following analysis, it is assumed that TIS_C

1) is comprised of ideal switches and inductors;
2) the switching functions *K(d)*, *K(d')*, and *K(d_c)* are ideally synchronized;
3) the leakage current is discontinuous;
4) the voltage sources v_0, v_1, v_2, and v_C, connected to TIS_C terminals, are ideal.

2) Derivation of TIS_C Model in CCM: TIS_C waveforms in Fig. 5 show that commutation intervals affect the volt-sec balance of the magnetizing inductance as well as the distribution of the magnetizing current between TIS_C's terminals in CCM.

Examining the waveforms in Fig. 5, see also Fig. 4(b) and (c), reveals that during the turn-ON interval the leakage current ramps up from zero and by the end of the on interval equals the peak magnetizing inductor current, i_{pk}. The total amount of volt-sec required by the leakage during the ON time is $L_{lk}i_{pk}$. The leakage does not affect the OFF-time volt-sec of the magnetizing inductance, see Fig. 4(d) and (e). Therefore, accounting for the "snipped" volt-sec the average voltage across the magnetizing inductance can be expressed by the following:

$$v_{Lm} = dv_{10} + ad'v_{20} - f_s L_{lk} i_{pk} \tag{1}$$

where, as usual, *d* is the ON duty cycle; *d' = 1-d* is the OFF duty-cycle, and $f_s = \frac{1}{T_s}$ is the switching frequency.

Examining Figs. 4 and 5, the peak current ripple of the magnetizing inductance, Δi_{Lm}, can be approximated by the following:

$$\Delta i_{Lm} = \frac{dv_{10}}{2f_s\left(L_m + L_{lk}\right)}. \tag{2}$$

Therefore, the peak magnetizing inductor current is as follows:

$$i_{pk} = i_{Lm} + \Delta i_{Lm} = i_{Lm} + \frac{dv_{10}}{2f_s\left(L_m + L_{lk}\right)}. \tag{3}$$

The considerations above suggest that the volt-sec balance of the magnetizing inductance can be approximated by the following:

$$v_{Lm} \approx dv_{10} + ad'v_{20} - f_s L_{lk}\left[i_{Lm} + \frac{dv_{10}}{2f_s\left(L_m + L_{lk}\right)}\right]. \tag{4}$$

Whence, the magnetizing current can be derived as follows:

$$i_{Lm} = \frac{1}{r + sL_m} v_{Lm}. \tag{5}$$

Here, *r* is the parasitic resistance of the TIS block [29].

Further examination of the terminal currents in Fig. 5 reveals that due to the turn-ON commutation a triangular segment is lost to the active switch current, i_1. This segment, however, augments the output current, i_2. Similarly, but, to a much greater extent, the turn-OFF commutation reduces the current i_2/a while increasing the i_C current by the same amount. Thus, for the sake of simplicity, only the turn-OFF commutation effect will be considered.

During the turn-OFF commutation interval, the current of the leakage inductance flows through the clamp terminal *C*, see Figs. 4(c) and 5. Therefore, the duration of the turn-OFF commutation interval is as follows:

$$\Delta t = L_{lk} i_{pk} / \left(v_C + av_{20}\right) \tag{6}$$

and the average current of the clamp terminal is as follows:

$$i_C = \frac{1}{2}\frac{i_{pk}\Delta t}{T_s} = \frac{1}{2} f_s L_{lk} \frac{\left(i_{Lm} + \frac{dv_{10}}{2f_s\left(L_m + L_{lk}\right)}\right)^2}{v_C + av_{20}}. \tag{7}$$

According to the considerations above, and neglecting the turn-ON commutation, the terminals' currents can be approximated as follows:

$$i_1 \approx di_{Lm} \tag{8}$$

$$i_2 \approx ad'i_{Lm} - ai_C \tag{9}$$

$$i_0 = i_1 + i_2 + i_C. \tag{10}$$

Equations (1)–(10) can be considered as the large-signal model of the TIS_C block. Apparently, only two terms are needed to incorporate the derived above leakage model into the ideal TIS model [29]. Yet, due to its nonlinear nature and a number of variables involved in generating the clamp current, i_C, (7), the leakage model introduces noticeable differences.

The steady-state TIS_C model can be readily derived from the large-signal model (1)–(10) as follows:

$$\begin{cases} V_{Lm} = V_{10}D + V_{20}aD' - \left(I_{Lm} + \frac{DV_{10}}{2f_s\left(L_m + L_{lk}\right)}\right) f_s L_{lk} \\ I_C = \frac{1}{2} f_s L_{lk} \frac{\left(I_{Lm} + \frac{DV_{10}}{2f_s\left(L_m + L_{lk}\right)}\right)^2}{V_C + aV_{20}} \\ I_1 = I_{Lm} D \\ I_2 = aD'I_{Lm} - aI_C. \\ I_0 = I_1 + I_2 \ + I_{\rm c} \end{cases} \tag{11}$$

In the sake of simplicity, define the ripple factor of the magnetizing inductor current as follows:

$$k = \frac{i_{pk}}{i_{Lm}} = 1 + \frac{DV_{10}}{2I_{Lm} f_s\left(L_m + L_{lk}\right)}. \tag{12}$$

Recall that under ideal, ripple-less magnetizing current conditions $k \underset{L_m \to \infty}{\to} 1$, whereas on the borderline of continuous and discontinuous modes $k \underset{L_m \to L_{m\ crit}}{\to} 2$. Hence, $1 < k < 2$, so that, on average, $k \approx 1.5$ can be assumed.

Substituting (12) into (11), leads to the steady-state TIS_C SFG model shown in Fig. 6(b). Worthwhile noting that the leakage inductance creates a local negative feedback path, see Fig. 6, which restrains the average current of the magnetizing inductance. This can explain the damping effect of the leakage reported by [4], [26], see Fig. 2, that with increased leakage inductance lowers the resonance peak and brings about a gentler phase transition.

Furthermore, perturbing the large-signal CCM model (1)–(10) leads to the small-signal TIS_C model in Fig. 6(c), which results in the following set of equations:

$$\begin{cases} \hat{v}_{Lm} = \hat{v}_{10} D\left(1 - g_0\right) + \hat{v}_{20} a\left(1 - D\right) \\ \qquad -\hat{i}_{Lm} f_s L_{lk} + \left(V_{10} - g_0 V_{10} - aV_{20}\right)\hat{d} \\ \hat{i}_{Lm} = \frac{\hat{v}_{Lm}}{r + sLm} \\ \hat{i}_1 = D\hat{i}_{Lm} + I_{Lm}\hat{d} \\ \hat{i}_2 = a\left(1 - D\right)\hat{i}_{Lm} - aI_{Lm}\hat{d} - a\hat{i}_c \\ \hat{i}_0 = \hat{i}_1 + \hat{i}_2 + \hat{i}_c \\ \hat{i}_C = g_1\hat{i}_{Lm} + g_2\hat{v}_C + g_3\hat{v}_{20} + g_4\hat{d} + g_5\hat{v}_{10} \end{cases}. \tag{13}$$

Here, the gain functions are as follows:

$$\begin{cases} g_0 = \frac{L_{lk}}{2\left(L_m + L_{lk}\right)} \\ g_1 = \frac{\partial i_C}{\partial i_{Lm}} = f_s L_{lk} \frac{kI_{Lm}}{V_C + aV_{20}} \\ g_2 = -\frac{1}{2} f_s L_{lk} \frac{k^2 I_{Lm}^2}{\left(V_C + aV_{20}\right)^2} \\ g_3 = -\frac{1}{2} a f_s L_{lk} \frac{k^2 I_{Lm}^2}{\left(V_C + aV_{20}\right)^2} \\ g_4 = g_0 V_{10} \frac{kI_{Lm}}{V_C + aV_{20}} \\ g_5 = g_0 D \frac{kI_{Lm}}{V_C + aV_{20}}. \end{cases} \tag{14}$$

3) Derivation of TIS_C Model in DCM: The key waveforms of TIS_C in DCM are shown in Fig. 7. Since the current, i_2, ramps down to zero at the end of the OFF-interval, there is no commutation interval between i_1 and i_2 (in contrast to CCM scenario, see Fig. 4). The equivalent circuits for the three operation subintervals are illustrated in Fig. 8.

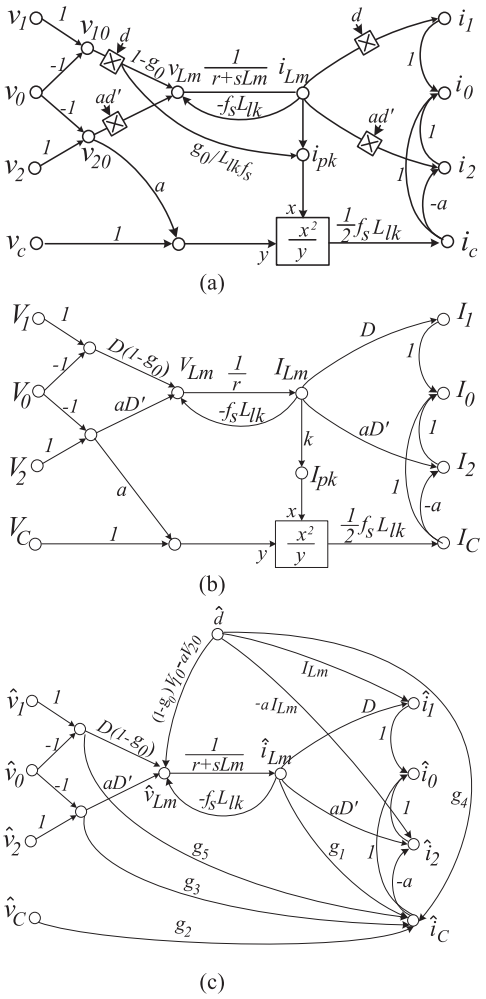

Fig. 6. TIS_C's equivalent SFG models (CCM). (a) Large-signal model. (b) Steady-state model. (c) Small-signal model.

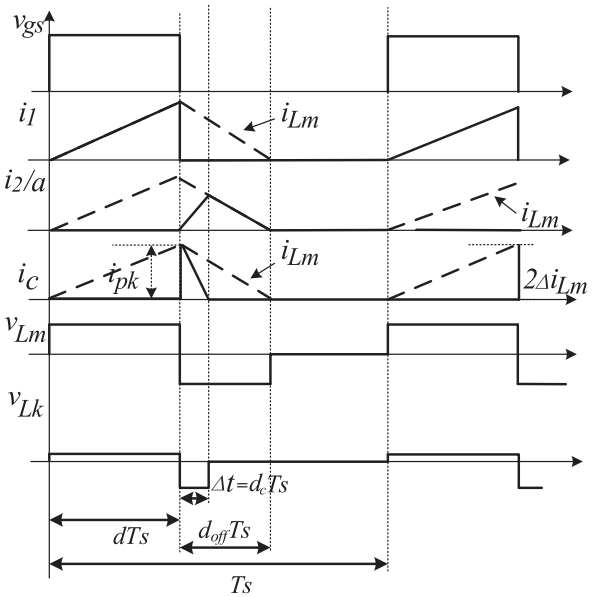

Fig. 7. Key waveforms of the TIS_C in discontinuous current mode (DCM). (*Vc* represents the clamp voltage).

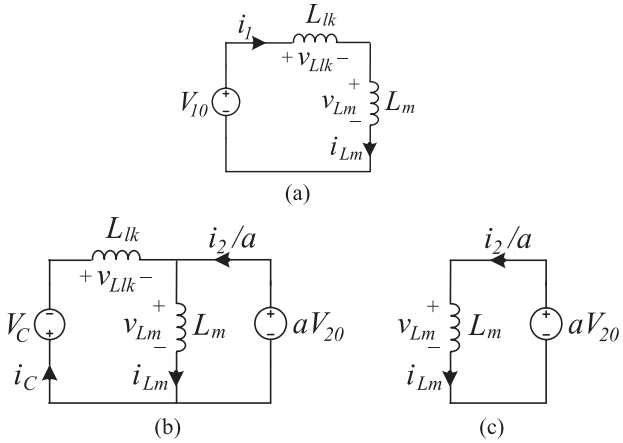

Fig. 8. TIS_C's equivalent circuits operated in DCM mode. (a) ON-state (charging of L_m). (b) ON–OFF commutation interval. (c) OFF-state (discharging of L_m).

First, as shown in Fig. 7, during the ON-state, the current of terminal *1*, i_1, equals the magnetizing current, i_{Lm}, see Fig. 8(a). The averaged value of i_1 can be derived as follows:

$$i_1 = \frac{1}{2} d i_{pk}. \tag{15}$$

Here, i_{pk} is the peak value of the magnetizing current i_{Lm}, which can be attained as follows:

$$i_{pk} = \frac{dv_{10}}{f_s\left(L_m + L_{lk}\right)}. \tag{16}$$

Next, as the active switch is turned OFF, the current of the leakage inductance is steered to flow through the clamp terminal *C*, see Fig. 8(b). The duration of this interval was obtained in (6). The averaged clamp current during DCM model can be attained by substituting (6) and (16) into (7) as follows:

$$i_C = \frac{1}{2}\frac{i_{pk}\Delta t}{T_s} = \frac{1}{2}\frac{f_s L_{lk} {i_{pk}}^2}{(av_{20} + v_c)} \tag{17}$$

Examining Figs. 7, 8(b) and (c) reveals that the average current of the terminal 2 current, i_2, is as follows:

$$i_2 = \frac{1}{2} a d_{\text{off}} i_{pk} - a i_C. \tag{18}$$

Whereas the averaged magnetizing current and voltage can be derived according to Fig. 8 as follows:

$$i_{Lm} = \frac{1}{2} i_{pk}\left(d + d_{\text{off}}\right) \tag{19}$$

$$v_{Lm} = d v_{10}\frac{L_m}{L_m + L_k} + a d_{\text{off}} v_{20}. \tag{20}$$

Substituting (19) into (15) and (18) leads to the following:

$$i_1 = \frac{d}{d + d_{\text{off}}} i_{Lm} \tag{21}$$

$$i_2 = a\frac{d_{\text{off}}}{d + d_{\text{off}}} i_{Lm} - a i_C \tag{22}$$

Here, $d_{\text{off}} = 2 f_s L_m \frac{i_{Lm}}{dv_{10}} - d$.

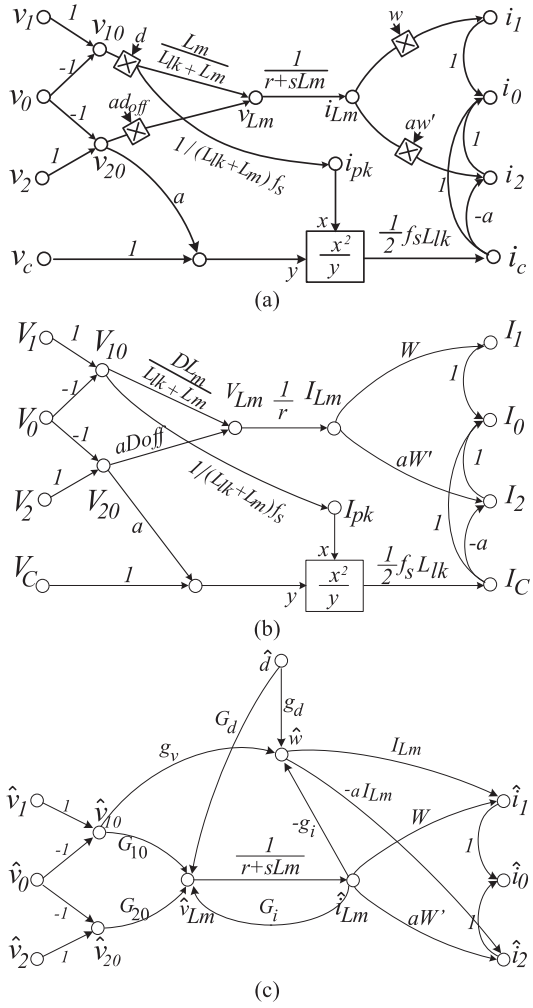

Fig. 9. TIS_C's equivalent SFG models for the DCM operational mode. (a) Large-signal model. (b) Steady-state model. (c) Small-signal model.

Introducing the definition of the weighting functions for current steering

$$\begin{cases} w = \frac{d}{d+d_{\text{off}}} \\ w' = \frac{d_{\text{off}}}{d+d_{\text{off}}} = 1 - w \end{cases} \tag{23}$$

and substituting into (15)–(22) the large-signal model of TIS_C in DCM can be obtained as follows:

$$\begin{cases} v_{Lm} = dv_{10}\frac{L_m}{L_m+L_k} + ad_{off}v_{20} \\ i_{Lm} = v_{Lm}/\left(r + sL_m\right) \\ i_0 = i_1 + i_2 + i_C \\ i_1 = wi_{Lm} \\ i_2 = aw'i_{Lm} - ai_C \\ i_C = \frac{d^2{v_{10}}^2 L_{lk}}{2(av_{20}+v_c)f_s(L_m+L_{lk})^2} = \frac{v_C}{Z_C}. \end{cases} \tag{24}$$

Here, r is the parasitic resistance of the TIS block, see [29]. The resulting switching-flow-graph (SFG) large-signal model of TIS in DCM is shown in Fig. 9(a).

The quiescent value of weighting function w in (24) is as follows:

$$W = \frac{1}{2f_sL_m}\frac{D^2V_{10}}{I_{Lm}}. \tag{25}$$

Whereas its small-signal perturbation can be found as follows:

$$\hat{w} = g_{\text{d}}\hat{d} + g_{\text{v}}\hat{v}_{10} - g_{\text{i}}\hat{i}_{Lm}. \tag{26}$$

Here, the gain coefficients are as follows:

$$g_{\text{d}} = \frac{1}{f_sL_m}\frac{DV_{10}}{I_{Lm}}$$

$$g_{\text{v}} = \frac{1}{2f_sL_m}\frac{D^2}{I_{Lm}}$$

$$g_{\text{i}} = \frac{1}{2f_sL_m}\frac{D^2V_{10}}{I_{Lm}^2}.$$

The small-signal perturbation of the voltage across the magnetizing inductor v_{Lm} can also be found

$$\hat{v}_{Lm} = G_d\hat{d} + G_i\hat{i}_{Lm} + G_{10}\hat{v}_{10} + G_{20}\hat{v}_{20} \tag{27}$$

where the gain coefficients are given by the following:

$$G_{10} = D\,\frac{L_m}{L_m+L_k} - 2aV_{20}\frac{I_{Lm}f_sL_m}{DV_{10}{}^2}$$

$$G_{20} = aD\left(\frac{1}{W} - 1\right)$$

$$G_i = 2aV_{20}\frac{f_sL_m}{DV_{10}}$$

$$G_d = V_{10}\frac{L_m}{L_m+L_k} - aV_{20}\left(\frac{2I_{Lm}f_sL_m}{V_{10}D^2} + 1\right).$$

The above discussion leads to the following set of equations describing the small-signal model of TIS in the DCM operational mode:

$$\begin{cases} \hat{i}_{Lm} = \hat{v}_{Lm}/\left(r + sL_m\right) \\ \hat{i}_0 = \hat{i}_1 + \hat{i}_2 \\ \hat{i}_1 = W\hat{i}_{Lm} + I_{Lm}\hat{w} \\ \hat{i}_2 = a\left(1-W\right)\hat{i}_{Lm} - aI_{Lm}\hat{w} \\ \hat{v}_{Lm} = G_d\hat{d} + G_i\hat{i}_{Lm} + G_{10}\hat{v}_{10} + G_{20}\hat{v}_{20} \\ \hat{w} = g_{\text{d}}\hat{d} + g_{\text{v}}\hat{v}_{10} - g_{\text{i}}\hat{i}_{Lm}. \end{cases} \tag{28}$$

Note that since $L_{lk} \ll (L_m + L_{lk})^2$, the perturbance of i_C is rather small. Moreover, considering the relatively long time constant of the RCD clamp circuit, the variations in $\hat{i}_c$ and $\hat{v}_c$ can be neglected in some cases. The considerations above allow constructing the simplified small-signal SFG model of the TIS_C block for DCM mode of operation as shown in Fig. 9(c).

III. Application Example: The Flyback Converter

A typical Flyback converter with an RCD clamp, shown in Fig. 10, operated in CCM mode was chosen as a study case. Here, the source voltage is $V_{10} = V_g$, the clamp is comprised of the diode D_c, clamp capacitor $\text{C}_\text{c,}$ and clamp discharge resistor R_C. The capacitive output filter is C_O, with the associated equivalent

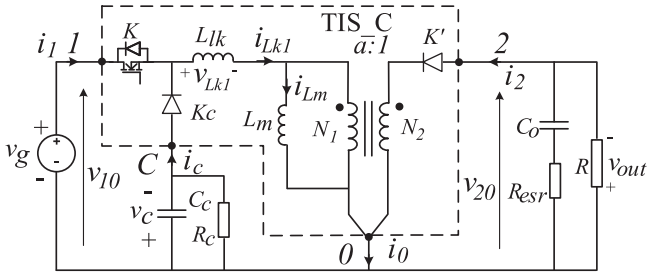

Fig. 10. Study case: The Flyback converter with RCD clamp.

series resistance $R_{\rm esr}$. The load resistance is designated as R. The effective turns ratio is $a = \frac{N_{10}}{N_{20}} = \frac{1}{n}$.

The application of the proposed unified model is rather simple and unfolds as follows.

The first step of the modeling procedure starts referring to Fig. 10, by identifying the switcher module terminals (0, 1, 2), see the dashed box.

The second step only requires to correctly assign the voltages $v_0 = 0$, $v_1 = v_g$, $v_2 = -v_{\rm out}$, and $v_{\rm out} = i_{2*} Z_{\rm out}$ to the TIS_C terminals in Fig. 6 (CCM models).

The third step, the TIS_C model is completed by introducing the load impedance and the clamp impedance $Z_{\rm out} = \frac{R(sC_oR_{esr}+1)}{sC_oR+sC_oR_{esr}+1}$, and the clamp, $Z_c = \frac{R_c}{sC_cR_c+1}$.

The resulting TIS_C models of the CCM Flyback converter are illustrated in Fig. 11. Noted, only a few (blue) branches have to be added to the prefabricated unified TIS_C modeling block in Fig. 6.

The steady-state solution of the Flyback converter in CCM can be obtained from Fig. 11(a) as follows:

$$V_C = \frac{R_c D V_g}{2D'^4 R^2 R_c + a_1}\left[k\left(k+1\right) D\prime R f_s n^2 L_{lk} + D'^3 R^2 + a_2 a_3\right] \tag{29}$$

$$V_{\rm out} = \frac{nRDV_g\{2D\prime R_c a_2 - k f_s L_{lk}[a_3 + (k-1)\, D\prime R]\}}{2D'^4 R^2 R_c + a_1} \tag{30}$$

$$I_{lm} = \frac{DV_g\left[2n^2 k f_s L_{lk}\left(n^2 R_c + R\right) + 2D'^2 R R_c n^2 + D'^2 R^2 - RD\prime a_3\right]}{2D'^4 R^2 R_c + a_1} \tag{31}$$

where

$$a_1 = 2k^2 n^2 {f_s}^2 {L_{lk}}^2\left(n^2 R_c + R\right) - k f_s L_{lk} D'^2 R \times \left[(k-2)\, R - 4n^2 R_c\right]$$

$$a_2 = k n^2 f_s L_{lk} + D'^2 R$$

$$a_3 = \sqrt{2k^2 n^2 f_s L_{lk}\left(R_c n^2 + R\right) + D'^2 R^2}.$$

The small-signal analytic model of the Flyback converter in CCM can be derived from Fig. 11(b) applying Mason's rule.

The model of the DCM Flyback can be obtained following the stated above analysis procedure, however, employing the DCM TIS_C model in Fig. 9.

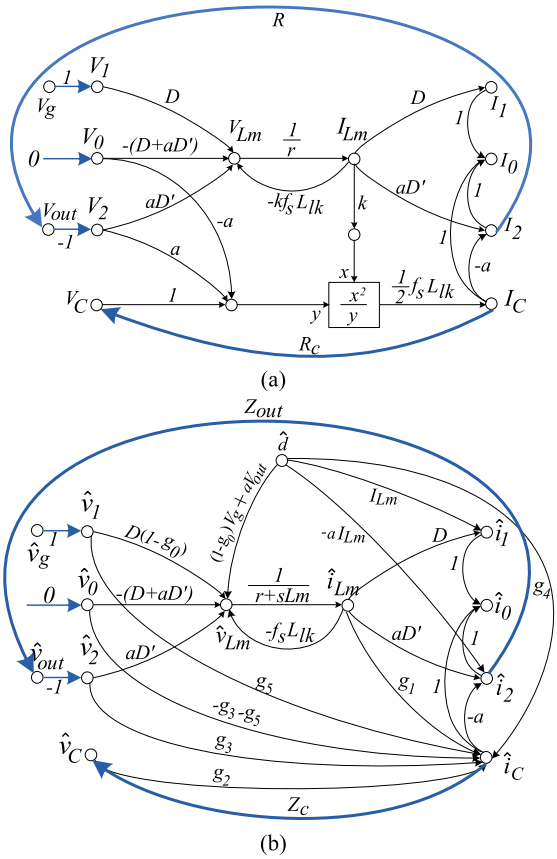

Fig. 11. TIS-SFG models of the CCM Flyback converter. (a) Steady-state model. (b) Small-signal model.

The steady-state solution of the DCM Flyback can be found by substitution of terminal assignments and load impedance into Fig. 9(b). The resulting nonideal voltage gain is as follows:

$$\frac{V_{\rm out}}{V_{\rm g}} = \frac{R}{2}\sqrt{\frac{{I_C}^2}{n^2 {V_g}^2} + \frac{2D^2}{R f_s\left(L_m + L_k\right)}} - \frac{I_C}{nV_g} \tag{32}$$

whence, an ideal voltage gain can be obtained substituting $I_C = 0$, $L_k = 0$, into (32). The following result corresponds to the following [13]:

$$\frac{V_{\rm out}}{V_{\rm g}} = D\sqrt{\frac{R}{2f_s L_m}}. \tag{33}$$

IV. Simulation Results

To verify the theoretical analysis, a benchmark Flyback converter was simulated in PSIM 9.14.

The parameters of the benchmark converter in PSIM were: $V_g = 100$ V, $C_o = 100$ μF, duty cycle $D = 0.39$, $R_{esr} = 0.18$ Ω, $f_s = 65$ kHz, The coupled inductor parameters were: $L_m = 715$ μH, $n = 0.28$. The RCD clamp parameters: $C_C = 1$ μF, $R_C = 10$ kΩ. The normalized leakage inductance L_{lk}/L_m was varied in the 0%–10% range (L_{lk}/L_m = [0–0.1]). The benchmark converter operated in CCM mode with a load $R = 10$ Ω, while operated in DCM with a load $R = 50$ Ω.

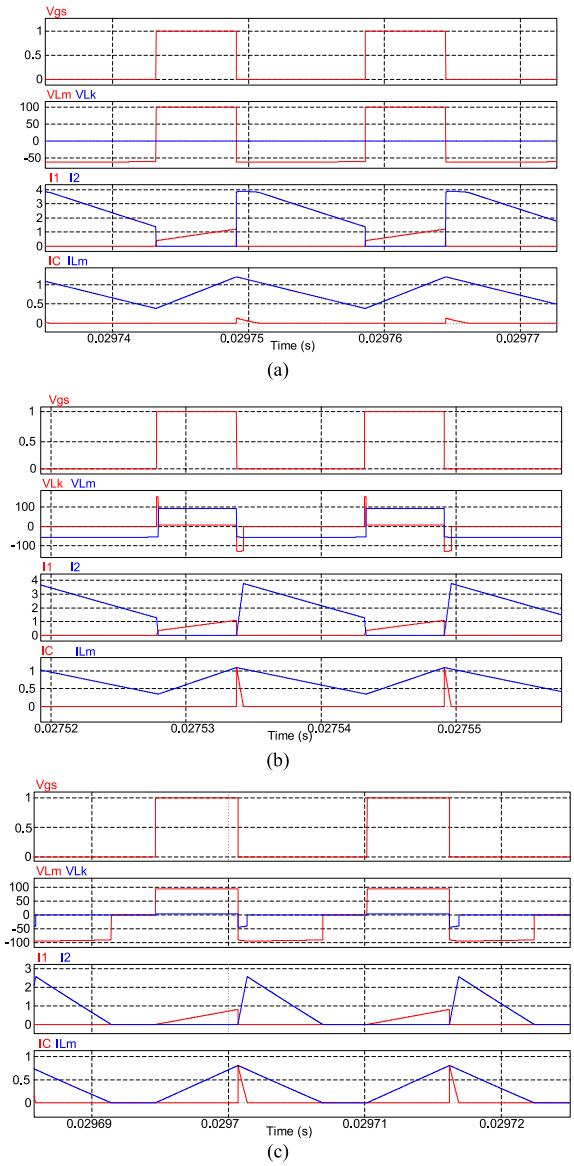

Fig. 12. TIS_C simulation study. (a) Key waveforms at $D = 0.39$ and $L_{lk} = 0$. (b) At $D = 0.39$ and $L_{lk} = 0.05L_m$, CCM mode. (c) At $D = 0.39$ and $L_{lk} = 0.05L_m$, DCM mode. Top trace—the gating voltage v_{gs}; second trace—the voltage across the leakage inductance and the magnetizing inductance; third trace—the currents of the switched terminals of the TIS_C block; bottom trace—the magnetizing inductance current and the clamp (leakage discharge) current.

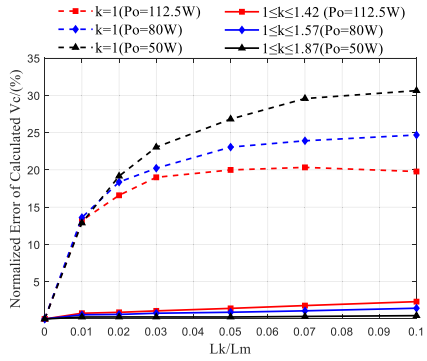

Fig. 13. Comparison of the simulated vs. the calculated clamp voltage V_c, as derived by the TIS_C model in CCM for an infinite L_m ($k = 1$) versus a finite L_m ($k \in [1, \quad 1.57]$) study cases $\left(err_{\rm v} = \frac{|{\rm V}_{Cpsim} - {\rm V}_{Ccalc}|}{{\rm V}_{Cpsim}} \times 100\%\right)$.

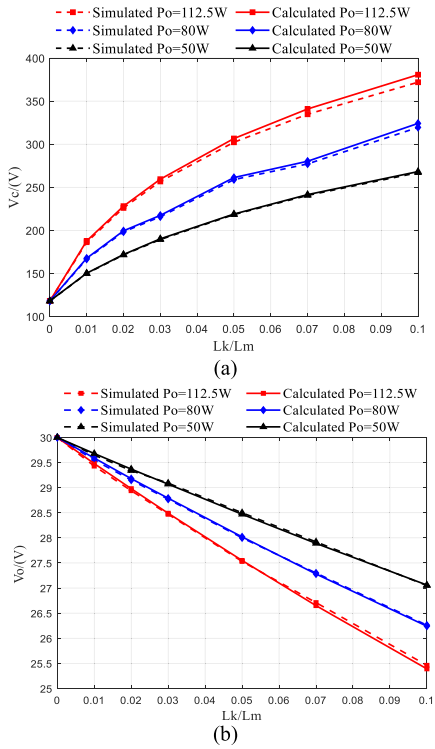

Fig. 14. Comparison of the calculated versus the simulated clamp voltage *Vc*, in CCM. (a) Output voltage $\rm V_{out}$. (b) ($L_m = 715\ \mu$H) considering magnetizing current ripple ($k \in [1, \quad 1.57]$).

The simulated waveforms in Fig. 12 illustrate the voltage across the leakage inductance and the magnetizing inductance; the currents of the switched terminals of the TIS block; the magnetizing inductance current and the clamp (leakage discharge) current and stand in agreement with Fig. 5.

Using the parameters above, the comparison of calculated versus the simulated clamp voltage V_c, was obtained as illustrated in Fig. 13. When the magnetizing current ripple is disregarded ($k = 1$) the calculation results produce a rather significant error, 20–30%, see the dashed line in Fig. 13. However, accounting for the magnetizing current ripple ($k \geq 1$) reduces the error to less than 2.5%, hence, greatly improving the accuracy of the calculated steady-state solution.

As shown in Fig. 14, the leakage has a significant impact on the steady-state solution of the circuit. For example, the clamp voltage is about 190V for $L_{lk}/L_m = 1\%$, increasing to 310 V for $L_{lk}/L_m = 5\%$. As shown in Fig. 14, an excellent agreement was found between the simulated output voltage and the theoretical prediction (29), (30). Thus, the proposed method can faithfully predict the steady state performance of the TI circuit.

Substituting the parameters above into the CCM small-signal model Fig. 11(b), the control-to-output voltage transfer function

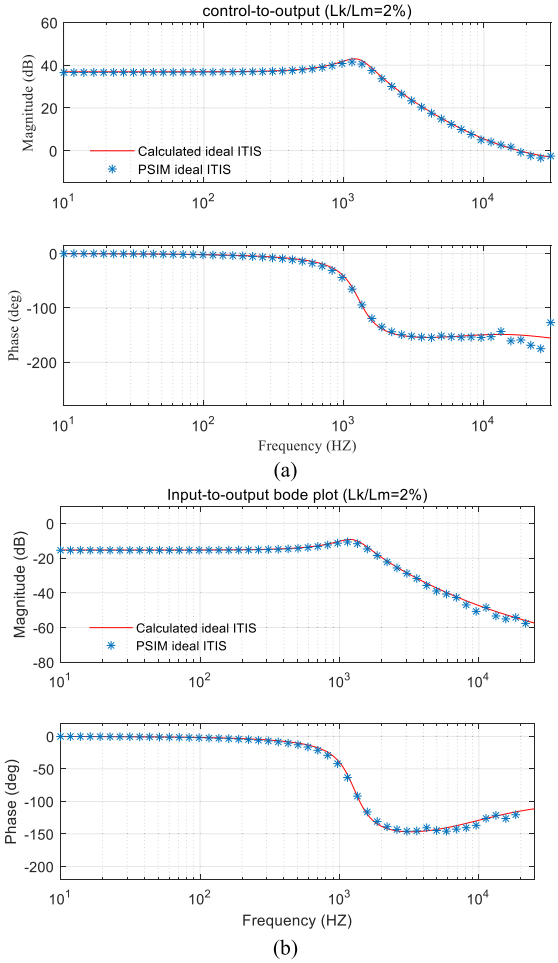

Fig. 15. Comparison of the calculated response by the proposed TIS_C versus (a) the simulated control-to-output frequency response (34) and (b) Input-to-output frequency response (35) of the Flyback converter.

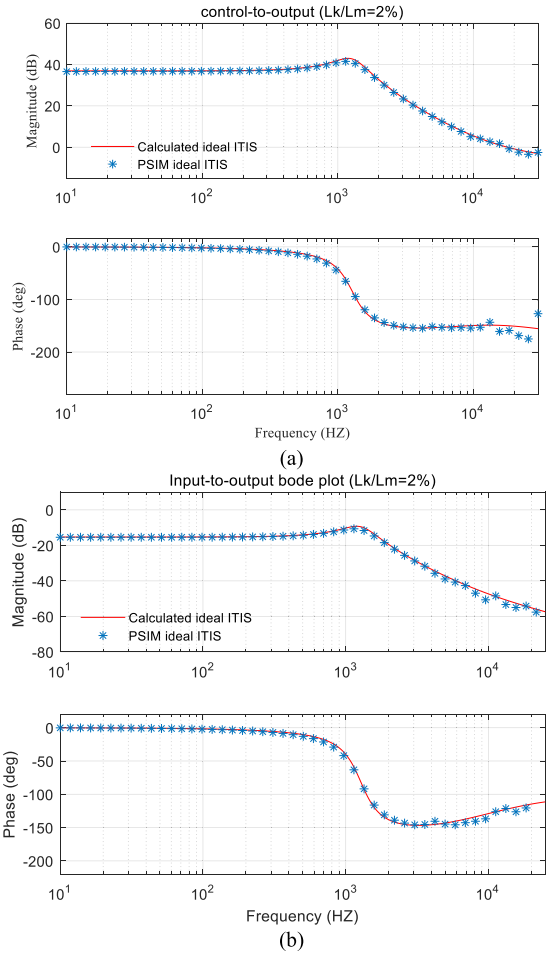

Fig. 16. Comparison of the simulated versus the calculated response obtained from the reduced-order small signal CCM model of the Flyback converter (36), (37): (a) control-to-output frequency response; and (b) input-to-output frequency response.

was obtained as follows (34) shown at the bottom of the next page.

The input-to-output voltage transfer function was obtained as follows (35) shown at the bottom of this page.

The comparison of the calculated CCM small-signal frequency response of the Flyback converter versus the simulated frequency responses is shown in Fig. 15. The theoretical results are well matched to the simulation results.

The impact of the snubber circuit on the converter response was considered next. In order to reduce the clamp voltage ripple, the time constant of the RCD clamp circuit normally is designed rather long. In such case the snubber has only a marginal effect on frequency response. Therefore, a reduced order small-signal model can be attained by neglecting the perturbations in the clamp voltage. Substituting $\hat{v}_c \approx 0$ into Fig. 11(b), the control to output voltage transfer function of the reduced order CCM small-signal model can be obtained as follows:

$$\frac{\hat{v}_{\text{out}}}{\hat{d}} = \frac{2.945 \times 10^{18} + 3.411 \times 10^{13} s - 3.401 \times 10^{8} s^2}{4.213 \times 10^{16} + 2.726 \times 10^{12} s + 6.522 \times 10^{8} s^2} \tag{36}$$

$$\frac{\hat{v}_{\text{out}}}{\hat{d}} = \frac{9.319 \times 10^{18} + 2.956 \times 10^{16} s + 3.401 \times 10^{11} s^2 - 3.403 \times 10^{6} s^3}{1.33 \times 10^{17} + 4.297 \times 10^{14} s + 2.926 \times 10^{10} s^2 + 6.522 \times 10^{6} s^3}. \tag{34}$$

$$\frac{\hat{v}_{\text{out}}}{\hat{v}_g} = \frac{2.286 \times 10^{16} + 7.266 \times 10^{13} s + 1.2728 \times 10^{7} s^2 - 497.087 s^3}{1.33 \times 10^{17} + 4.297 \times 10^{14} s + 2.926 \times 10^{10} s^2 + 6.522 \times 10^{6} s^3}. \tag{35}$$

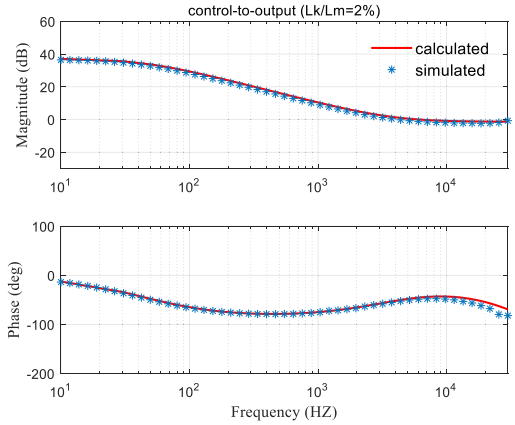

Fig. 17. Comparison of the simulated versus the calculated control-to-output frequency response from the reduced-order small-signal DCM model of the Flyback converter $D = 0.39$, $R_{\rm load} = 50\ \Omega$.

while the input-to-output voltage transfer function can be obtained as follows:

$$\frac{\hat{v}_{\rm out}}{\hat{v}_g} = \frac{70225 \times 10^{15} + 1.273 \times 10^{11} s - 49708.72671 s^2}{4.213 \times 10^{16} + 2.726 \times 10^{12} s + 6.522 \times 10^{8} s^2}. \tag{37}$$

Evidently, the proposed model of the benchmark Flyback converter (34) and (35) is of a third order, whereas the reduced model (36) and (37) is only of the second order and is easier to handle.

The comparison of the calculated reduced-order CCM small-signal frequency response of the Flyback converter versus the simulated frequency response is shown in Fig. 16 and stands in good agreement with the simulated results (obtained by PSIM 9.1.4). Therefore, the reduced model may be considered adequate and can be adopted for design purposes.

The DCM model in (24), (28), and (32) were also verified. The simulated nominalized error of the nonideal steady state output voltage gain in (32) is approximately 4%, in contrast the error of ideal voltage gain solution in (33) is around 10.5%.

The DCM small-signal model of the studied Flyback can be obtained by substitution of $v_{10} = v_g$, $v_{20} = -v_{\rm out}$, $v_{\rm out} = i_{2*} Z_{\rm out}$ into (28) results in the following:

$$\begin{cases} \hat{i}_{Lm} = \hat{v}_{Lm} / (r + sL_m) \\ \hat{i}_2 = \frac{(1-W)}{n} \hat{i}_{Lm} - \frac{I_{Lm}}{n} \hat{w} \\ \hat{v}_{Lm} = G_d \hat{d} + G_i \hat{i}_{Lm} + G_{10} \hat{v}_g - G_{20} \hat{v}_{\rm out} \\ \hat{w} = g_{\rm d} \hat{d} + g_{\rm v} \hat{v}_g - g_{\rm i} \hat{i}_{Lm} \\ \hat{v}_{\rm out} = \hat{i}_2 Z_{\rm out} \\ Z_{\rm out} = \frac{R(1+sC_o R_{esr})}{1+sC_o(R+R_{esr})}. \end{cases} \tag{38}$$

Substitution of the benchmark circuit parameters into (38) (in DCM the load value of $R = 50\ \Omega$was used) the small signal output-to-control transfer in DCM was found as follows:

$$\frac{\hat{v}_{\rm out}}{\hat{d}} = -\frac{1.387 \times 10^{-5} s^2 - 3.9645 \times 10^{9} s - 1.0227 \times 10^{5}}{1.614 \times 10^{-5} s^2 + 5.0364 s + 1396.95}. \tag{39}$$

The comparison of the calculated DCM small-signal frequency response of the Flyback converter versus the simulated frequency response is shown in Fig. 17.

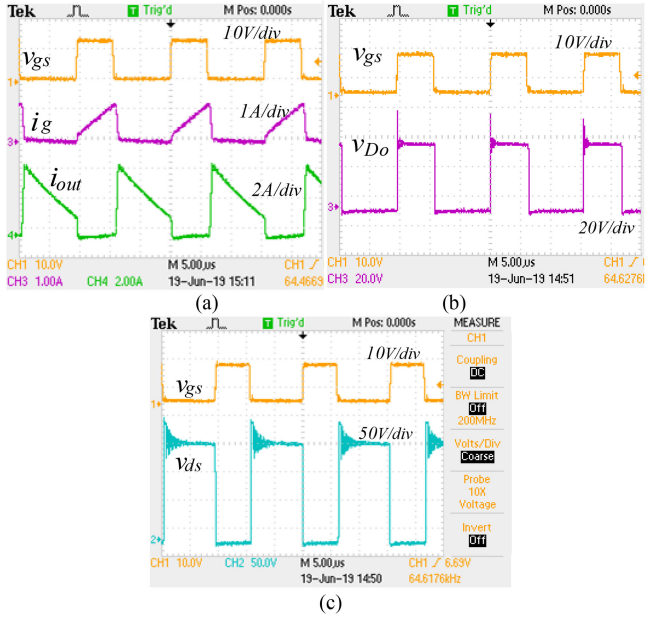

Fig. 18. Experimental waveforms of the prototype Flyback converter, the gating signal of the main switch, v_{gs}, the input current, i_g, and the output current, $i_{\rm out}$ (a); the gating signal $v_{\rm gs}$, and the diode voltage $v_{\rm do}$ (b); the gating signal $v_{\rm gs}$, and the switch voltage v_{ds} (c). Horizontal scale 5 μS.

V. Experimental Verification

To further confirm the proposed approach, a prototype Flyback converter was built and tested. The parameters of the prototype circuit were: $V_g = 100$ V; duty cycle $D = 0.39$; load resistor $R = 10\ \Omega$; output capacitor $C_o = 100\ \mu$F; $r_{esr} = 0.18\ \Omega$, $f_s = 64.8$ kH. The coupled inductor magnetizing inductance was: $L_m = 715\ \mu$H, $n = 0.28$, and the measured leakage inductance was $L_{lk} = 22.5\ \mu$H. The ripple coefficient was found according to (12) as $k = 1.51$.

The ideal voltage stress over the Main switch Q neglecting the leakage inductance is $(V_g + V_{\rm out}/n) = 163.9$ V. The clamp voltage was designed to 200 V. The RCD clamp was designed according to [4]. Clamp capacitance $C_C = 1\ \mu$F, and clamp resistor $R_C = 10$ kΩ were used.

When the prototype Flyback was operated in CCM mode, the measured output voltage was 16.92 V. The key experimental waveforms are shown in Fig. 18. Here, the voltage across the main switch, $V_{\rm ds}$, is nearly 210 V.

The frequency response of the prototype Flyback converter was measured by Venable 8805 frequency response analyzer. The comparison of the calculated versus the experimentally

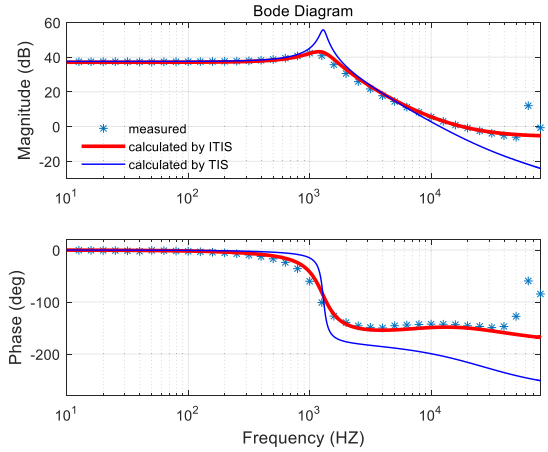

Fig. 19. Triple comparison of the experimentally measured small-signal duty-cycle to output voltage frequency response of the benchmark Flyback converter in CCM with RCD snubber versus the calculated by the proposed TIS_C model (34) versus the calculated by ideal (leakage-less) TIS model [29].

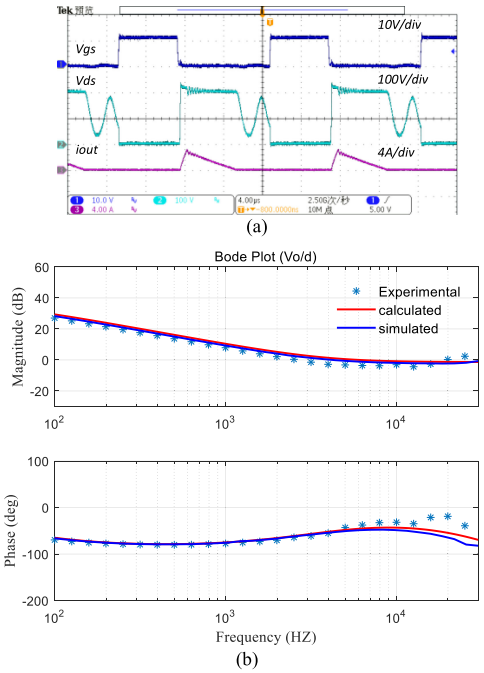

Fig. 20. Experimental results of the benchmark Flyback converter in DCM. (a) Tested key waveforms. (b) Comparison of the experimentally measured small-signal duty-cycle to output voltage frequency response of t versus the calculated by the proposed TIS_C model (39).

measured response is shown in Fig. 19 (CCM) and in Fig. 20 (DCM). A good agreement of the results was found. This supports the validity of the proposed modeling approach. The converter's response to the duty cycle step (from 0.345 to 0.42) is shown in Fig. 21.

The experimental platform is shown in Fig. 22.

VI. Conclusion

This article presented unified models for tapped inductor converters operating in CCM and DCM operational modes, which considers the leakage effects. The proposed models are

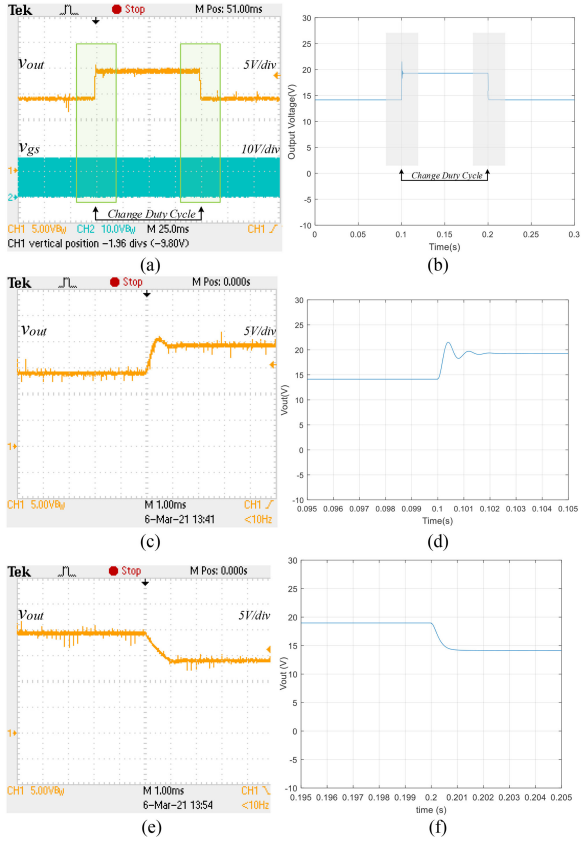

Fig. 21. Comparison of the (a), (c), (e) experimental versus the (b), (d), (f) calculated step response. (a), (b) output voltage response of the benchmark Flyback converter to stepped duty cycle (from 0.345 to 0.42 @ $V_{\text{in}} = 100$ V) Vertical scale 5 V/div; horizontal scale 0.05 s/div. Exploded view of the: rising edge transient (c), (d); and the falling edge transient (e), (f). Vertical scale 5 V/div; horizontal scale 1 ms/div.

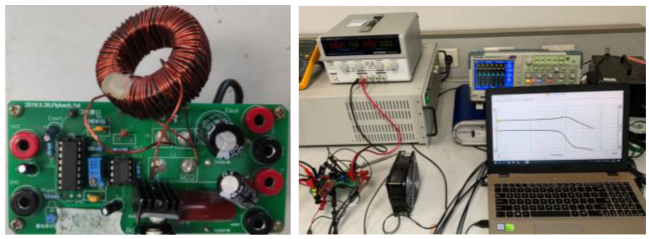

Fig. 22. View of the experimental set-up.

independent of power stage topology and can be used to predict the steady-state as well as small-signal behavior of a variety of converters employing a two-winding tapped inductor.

The proposed TIS_C model can accurately predict the steady-state and small-signal responses that stand in good agreement with both simulation and experimental results obtained from a benchmark converter.

Primarily, the proposed models are aimed to attain analytical results but, can also be easily applied and coded "as is" into MATLAB/SIMULINK simulation package to produce frequency response plots of a problem converter.

The proposed TIS_C SIMULINK models, which can help attain fast modeling of PWM dc–dc converters and facilitate the controller design, were uploaded and made available to MATLAB community [31].

APPENDIX

TABLE II
IDENTIFYING THE TIS_C'S TERMINALS IN BASIC TAPPED INDUCTOR CONVERTERS

	Buck-derived	Boost-derived	Buck-Boost- derived
Switch to tap	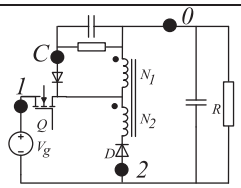 $a = 1/(1+n)$	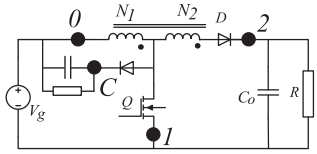 $a = 1/(1+n)$	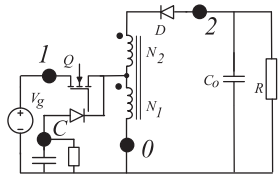 $a = 1/(1+n)$
Diode to tap	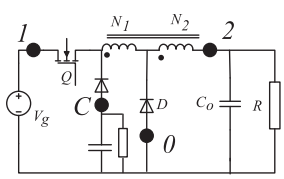 $a = 1 + 1/n$	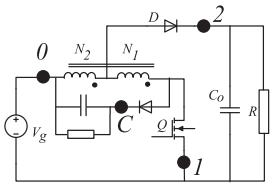 $a = 1 + 1/n$	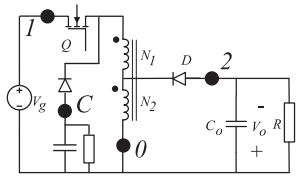 $a = 1 + 1/n$
Rail to tap	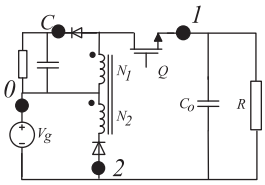 $a = -1/n$	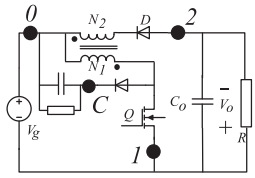 $a = -1/n$	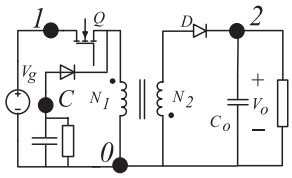 $a = -1/n$

REFERENCES

[1] D. A. Grant and Y. Darroman, "Extending the tapped-inductor DC-to-DC converter family," *Electron. Lett.*, vol. 37, no. 3, pp. 145–146, Feb. 2001.

[2] N. Vazquez, L. Estrada, C. Hernandez, and E. Rodriguez, "The tapped-inductor boost converter," in *Proc. IEEE Int. Symp. Ind. Electron.*, 2007, pp. 538–543.

[3] H. Wu, K. Sun, L. Chen, L. Zhu, and Y. Xing, "High step-up/step-down soft-switching bidirectional DC–DC converter with coupled-inductor and voltage matching control for energy storage systems," *IEEE Trans. Ind. Electron.*, vol. 63, no. 5, pp. 2892–2903, May 2016.

[4] C. Basso, "How to deal with leakage elements in flyback converters," Sep. 2005. [Online]. Available: https://www.onsemi.com/pub/Collateral/AN1679-D.PDF

[5] Z. Ouyang, O. C. Thomsen, and M. A. E. Andersen, "The analysis and comparison of leakage inductance in different winding arrangements for planar transformer," in *Proc. Int. Conf. Power Electron. Drive Syst.*, 2009, pp. 1143–1148.

[6] Colonel Wm. T. McLyman, "Winding capacitance and leakage inductance," in *Transformer and Inductor Design Handbook*, 4th ed., Chap. 17, Boca Raton, USA: CRC Press, 2014, pp. 17.1–17.14.

[7] S. Ćuk and Z. Zhang, "Coupled-inductor analysis and design," in *Proc. 17th Annu. IEEE Power Electron. Spec. Conf.*, 1986, pp. 655–665.

[8] C. Vartak, A. Abramovitz, and K. M. Smedley, "Analysis and design of energy regenerative snubber for transformer isolated converters," *IEEE Trans. Power Electron.*, vol. 29, no. 11, pp. 6030–6040, Nov. 2014.

[9] M. Mohammadi, E. Adib, and M. R. Yazdani, "Family of soft-switching single-switch PWM converters with lossless passive snubber," *IEEE Trans. Ind. Electron.*, vol. 62, no. 6, pp. 3473–3481, Jun. 2015.

[10] J. Li, F. B. M. van Horck, B. J. Daniel, and H. J. Bergveld, "A high-switching-frequency flyback converter in resonant mode," *IEEE Trans. Power Electron.*, vol. 32, no. 11, pp. 8582–8592, Nov. 2017.

[11] A. S. Raj, A. M. Siddeshwar, K. P. Guruswamy, C. M. Maheshan, and C. V. Sanekere, "Modelling of flyback converter using state-space averaging technique," in *Proc. IEEE Int. Conf. Electron., Comput. Commun. Technol.*, 2015, pp. 1–5.

[12] A. Abramovitz, C. Liao, and K. Smedley, "State-plane analysis of regenerative snubber for flyback converters," *IEEE Trans. Power Electron.*, vol. 28, no. 11, pp. 5323–5332, Nov. 2013.

[13] R. W. Erickson and D. Maksimovic, *Fundamentals of Power Electronics*. New York, NY, USA: Springer, 2007.

[14] J. Duarte, L. R. Lima, L. Oliveira, M. Mezaroba, L. Michels, and C. Rech, "Modeling and digital control of a single-stage step-up/down isolated PFC rectifier," *IEEE Trans. Ind. Informat.*, vol. 9, no. 2, pp. 1017–1028, May 2013.

[15] S. Xu, Q. Qian, B. Ren, and Q. Liu, "An accurate small-signal modeling and control loop design of active clamp flyback converter," in *Proc. 10th Int. Conf. Power Electron.*, 2019, pp. 3259–3264.

[16] H. Kewei, L. Jie, F. Ningjun, L. Yuebin, H. Xiaolin, and W. Luo, "Modeling analysis and simulation of a high-voltage flyback DC-DC converter," in *Proc. IEEE Int. Symp. Ind. Electron.*, 2009, pp. 813–818.

[17] G. Zhu, B. A. McDonald, and K. Wang, "Modeling and analysis of coupled inductors in power converters," *IEEE Trans. Power Electron.*, vol. 26, no. 5, pp. 1355–1363, May 2011.

[18] S. Chakraborty, M. Palmal, and S. Chattopadhyay, "Approaches for continuous-time dynamic modeling of the asymmetric dual-active half-bridge converter," in *Proc. IEEE Appl. Power Electron. Conf. Expo.*, 2018, pp. 952–958.

[19] C.-Y. Chang, W.-s. Liu, and J.-F. Chen el, "Modified PWM switch model for continuous conduction mode DC–DC converters with coupled inductors," *IET Power Electron.*, vol. 3, no. 4, pp. 629–636, 2010.

[20] M. Das and V. Agarwal, "Generalized small signal modeling of coupled inductor based high gain, high efficiency DC-DC converters," in *Proc. IEEE Appl. Power Electron. Conf. Expo.*, 2015, pp. 2691–2695.

[21] S. Hasanpour, A. Baghramian, and H. Mojallali, "Reduced-order small signal modelling of high-order high step up converters with clamp circuit and voltage multiplier cell," *IET Power Electron.*, vol. 12, no. 13, pp. 3539–3554, 2019.

[22] M. Chen and J. Sun, "Reduced-order averaged modeling of active-clamp converters," *IEEE Trans. Power Electron.*, vol. 21, no. 2, pp. 487–494, Mar. 2006.

[23] P. Athalye, D. Maksimovic, and R. Erickson, "Averaged switch modeling of active-clamped converters," in *Proc. 27th Annu. Conf. IEEE Ind. Electron. Soc.*, 2001, vol. 2, pp. 1078–1083.

[24] K. Rustom, W. Qiu, C. Lannello, and I. Batarseh, "Unified flyback switching-cell model including the leakage inductance effects for SPICE simulation," in *Proc. IEEE 34th Annu. Conf. Power Electron. Spec.*, 2003, vol. 3, pp. 1215–1219.

[25] K. Rustom, W. Qiu, C. Iannello, and I. Batarseh, "Five-terminal switched transformer average modeling and AC analysis of PFC converters," *IEEE Trans. Power Electron.*, vol. 22, no. 6, pp. 2352–2362, Nov. 2007.

[26] C. Basso, "The flyback converter with leakage inductance part I–Hardware description," 2015. [Online]. Available: https://cbasso.pagesperso-orange.fr/Downloads/Papers/Flyback%20Converter%20with%20Leakage.pdf

[27] R. Tymember, A. Vorperian, and F. C. Lee, "Nonlinear modeling of the PWM switch," *IEEE Trans. Power Electron.*, vol. 4, no. 2, pp. 225–233, Apr. 1989.

[28] A. Davoudi, J. Jatskevich, and T. De Rybel, "Numerical state-space average-value modeling of PWM DC-DC converters operating in DCM and CCM," *IEEE Trans. Power Electron.*, vol. 21, no. 4, pp. 1003–1012, Jul. 2006.

[29] A. Abramovitz, J. Yao, and K. Smedley, "Unified modeling of PWM converters with regular or tapped inductors using TIS-SFG approach," *IEEE Trans. Power Electron.*, vol. 31, no. 2, pp. 1702–1716, Feb. 2016.

[30] J. Yao, K.W. Li, K. Zheng, and A. Abramovitz, "On the equivalence of the switched inductor and the tapped inductor converters and its application to small signal modelling," *Energies*, vol. 12, no. 24, pp. 4806–4818, Sep. 2019.

[31] J. Yao and A. Abramovitz, TIS_C Simulation Model. Mar. 2022. [Online]. Available: https://ww2.mathworks.cn/matlabcentral/fileexchange/98954-dc-dc-converter-modeling-toolbox-tis